Electronic Supplementary Material (ESI) for Journal of Materials Chemistry A.

Electronic Supplementary Information

Plasma-grown Graphene Petals Templating Ni-Co-Mn hydroxide Nanoneedles for High-rate and Long-cycle-life Pseudocapacitive Electrodes

Guoping Xiong,[a,b] Pingge He,[a,b,c] Lei Liu,[c] Tengfei Chen[c] and Timothy S. Fisher*[a, b]

[a]*Birck Nanotechnology Center, Purdue University, West Lafayette, IN 47907, USA.*

[b]*School of Mechanical Engineering, Purdue University, West Lafayette, IN 47907, USA.*

[c]*State Key Laboratory of Powder Metallurgy, Central South University, Changsha 410083, China.*

Experimental details:

Preparation of GPs on carbon cloth (CC/GPs): Commercial carbon cloth (CC, Fuel Cell Earth type CCP), washed in 6 M HNO_3 for 30 min to eliminate ash or contaminated residuals and dried at 100°C overnight, was used as the substrate to grow GPs through microwave plasma chemical vapor deposition (MPCVD), which has been previously described in detail elsewhere.[1-4] A schematic diagram of the experimental setup for GP growth is shown in Figure S1.[1] The plasma source is a 2.45 GHz frequency microwave power supply with variable power. Carbon cloth substrates (5×10 mm^2), elevated 7 mm above a 55-mm-diameter Mo puck by ceramic spacers, were subjected to MPCVD conditions of H_2 (50 sccm) and CH_4 (10 sccm) as the primary feed gases at 25 Torr total pressure. The substrates were initially exposed to hydrogen plasma for approximately 2 min, during which the plasma power gradually increased from 300 to 550 W. This process does not rely on additional external heating sources but the self-heating of plasma to ramp the temperature from room temperature to approx. 1000°C, as measured by a dual-wavelength pyrometer (Williamson PRO 92). The GP growth time was 15 min to ensure the CC substrates were fully covered by GPs.

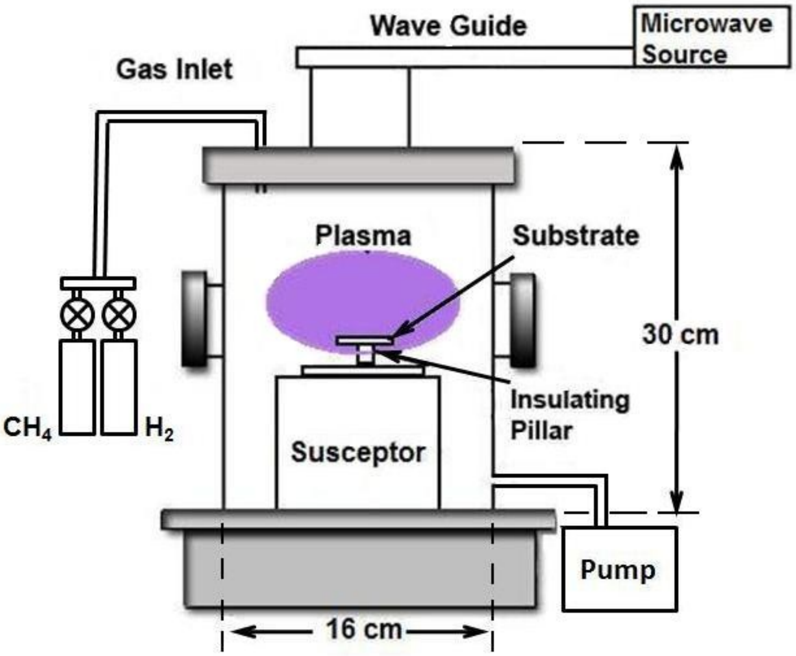

Fig. S1 Schematic diagram of the MPCVD chamber illustrating the approximate dimensions and positions of the substrate with respect to the plasma, reprinted with permission.[1]

***Synthesis of Ni-Co-Mn triple hydroxide (NCMTH) nanoneedles on CC/GPs*:** The solution with a volume of 14 mL was then transferred into a 20 mL Teflon-lined stainless steel autoclave. A piece of CC/GP substrate (5×10 mm^2) was first soaked in alcohol and then washed with purified water (pH = 7) thoroughly to fully wet the substrate surface before being transferred to the autoclave filled with the precursor solution. The autoclave was kept at 135 ˚C for 90 min in an electric oven and subsequently cooled to room temperature in air naturally. The samples were washed many times and sonicated to remove excessive metal hydroxides on CC/GPs. After cleaning, the samples were dried in air at a temperature of 80 ˚C for 3 hrs. The mass of metal hydroxides was measured by the weight difference before and after the hydrothermal process using a microbalance with an accuracy of 1 μg.

To elucidate the influence of Mn on the electrochemical performance of the triple-component metal hydroxides, we prepared Ni-Co double hydroxides (NCDHs) by a similar procedure as a reference electrode material. The precursor solution of NCDHs was prepared using 2.91 g $Co(NO_3)_2 \cdot 6H_2O$, 1.45 g $Ni(NO_3)_2 \cdot 6H_2O$ and 0.9 g urea as raw chemicals.[5] CC/NCMTHs and CC/GPs/NCDHs were prepared by a hydrothermal process under the same reaction conditions as CC/GPs/NCMTHs.

The specific capacitance of the electrodes is calculated from the charge/discharge curves based on: [6-8]

$$C_m = (I \times \Delta t) / (\Delta V \times m) \qquad (1)$$

where C_m (F g^{-1}) is the specific capacitance, I (A) is the applied current, Δt (s) is the discharge time, ΔV (V) is the potential change after IR drop during the discharge, and m (g) is the mass of active materials.

Energy density E (Wh kg^{-1}) and power density P (kW kg^{-1}) derived from galvanostatic charge/discharge tests are calculated from:

$$E = CV^2 / 2m \qquad (2)$$

$$P=E/\Delta t \tag{3}$$

where V (V) is the applied voltage, C (F) is the capacitance, m is the mass of active materials and Δt (s) is the discharge time.

Coulombic efficiency (η) is the ratio of the number of unit charge inputs during charging compared to the number extracted during discharging, reflecting the charge storage efficiency of electrodes. A low coulombic efficiency is caused by significant loss in charge during secondary reactions, such as the electrolysis of water or other redox reactions in the system.[9] The coulombic efficiency measured in galvanostatic charge/discharge tests is calculated from:[2, 6]

$$\eta= Q_{discharge} / Q_{charge}= I\, t_{\mathrm{discharge}}/ I\, t_{\mathrm{charge}}= t_{\mathrm{discharge}}/ t_{\mathrm{charge}} \tag{4}$$

where I is the applied current during galvanostatic charge and discharge.

To investigate the effect of Mn on the structure of NCMTHs, different precursor solutions with Ni: Co: Mn molar ratios of 1:1:1, 1:1:2 and 1:1:5 were prepared. Fig. 2 shows that NCMTHs with different morphologies were grown on Ni foam surface in the foregoing precursors in a hydrothermal process. When the molar ratio of Ni, Co and Mn is 1:1:1, NCMTH nanoneedles cover on the Ni ligament surface over a large scale (see Fig. S2a). Such NCMTH nanoneedles present very sharp tips (see Fig. S2b), the same as those grown on CC/GP substrates. However, when the Mn content increases (Ni: Co: Mn = 1:1:2), the NCMTHs exhibit nanosheet structures, rather than nanoneedles (see Figs. S2c and S2d). From Figs. S2e and S2f, NCMTHs still remain as nanosheets when the molar ratio of Ni, Co and Mn reaches 1:1:5. These results indicate that NCMTH structure significantly changes from nanoneedles to nanosheets with increasing Mn content in the precursor solution.

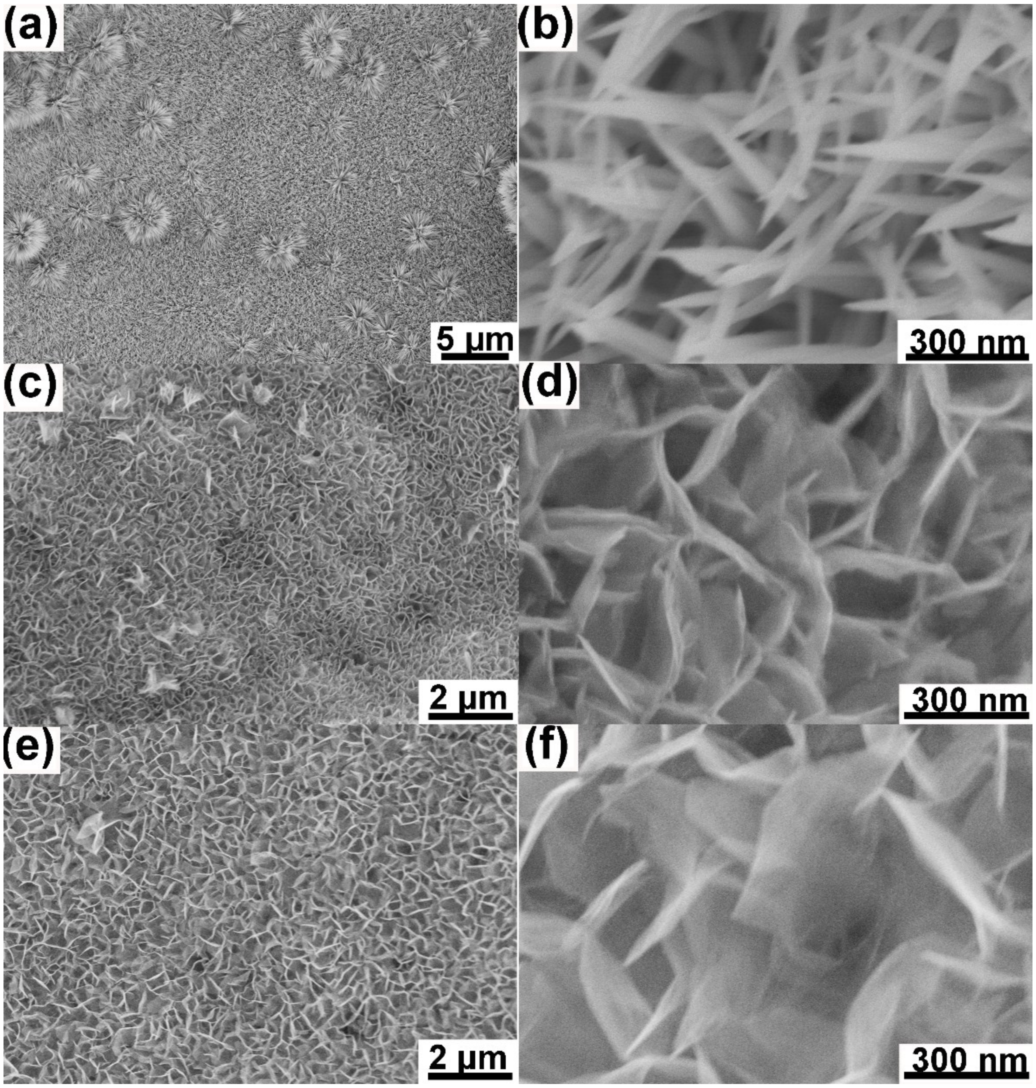

Fig. S2 SEM images of NCMTHs prepared in a series of precursor solutions with different Ni: Co: Mn molar ratios on Ni foam: a Ni: Co: Mn molar ratio of 1:1:1 (a) low magnification and (b) high magnification; a Ni: Co: Mn molar ratio of 1:1:2 (c) low magnification and (d) high magnification; a Ni: Co: Mn molar ratio of 1:1:5 (e) low magnification and (f) high magnification.

A similar morphology difference of NCMTHs with increasing Mn concentration has also been observed on CC/GP substrates. When the molar ratio of Ni, Co and Mn is 1:1:1, the GP surface is uniformly covered by NCMTH nanoneedles, forming the unique “needle-on-petal” structures (see Figs. S3a and S3b). With increased Mn content, NCMTHs present nanosheet structures (see Fig. S3c). Such vertical NCMTH nanosheets possess typical widths of a single, unwrinkled 2D petal ranging from 100 nm to 500 nm and thicknesses of a few nanometers (see Fig S3d). When the molar ratio of Ni, Co and Mn reaches 1:1:5, NCMTH nanosheets densely and uniformly cover the GP surface over a large scale. Combined with the previous results when using Ni foam as a substrate, we confirm that the content of Mn in the precursor solution has a deterministic effect on the structure and morphology of NCMTHs.

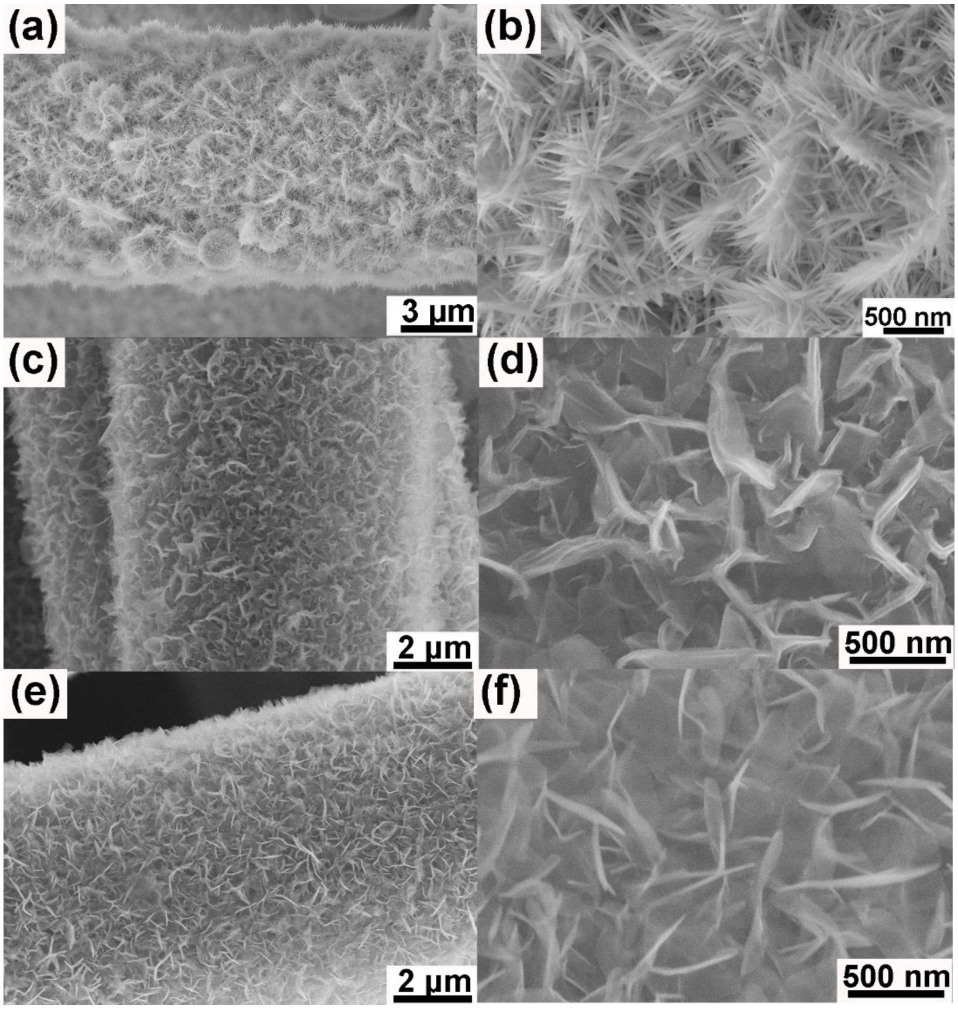

Fig. S3 SEM images of NCMTHs prepared in a series of precursor solutions with different Ni: Co: Mn molar ratios on CC/GPs: a Ni: Co: Mn molar ratio of 1:1:1 (a) low magnification and (b) high magnification; a Ni: Co: Mn molar ratio of 1:1:2 (c) low magnification and (d) high magnification; a Ni: Co: Mn molar ratio of 1:1:5 (e) low magnification and (f) high magnification.

The surface morphology of a bare CC substrate is shown in Fig. S4a and 4b. SEM images indicate that carbon fibers within the woven carbon tows possess diameters of approximately 9 µm. After growth of GPs, the carbon fiber surface is coated with a thin layer of uniform GPs, making it appear fluffy (roughened) (see Fig. S4c and 4d), as compared to the relatively smooth carbon fibers in bare CC (see Fig. S4a inset and Fig. S4b). Uniform, large-scale coverage of GPs on carbon fibers is shown in Fig. 4c and 4d. The high-magnification SEM image in Fig. S4e indicates that sharp and thin edges of GPs can be clearly distinguished, and GPs possess a typical width of a single, unwrinkled 2D petal ranging from 100 nm to 400 nm and a thickness of a few nanometers. The cross-sectional SEM image of CC/GPs reveals that GPs grow approximately 400 to 500 nm out from the carbon fiber surface (see Fig. S4f). According to BET studies of CC/GPs in prior work,[2] these GPs significantly improve the surface area of CC substrates, providing an excellent nanotemplate for pesudocapacitive materials and thus promoting more charge storage in the electrodes.

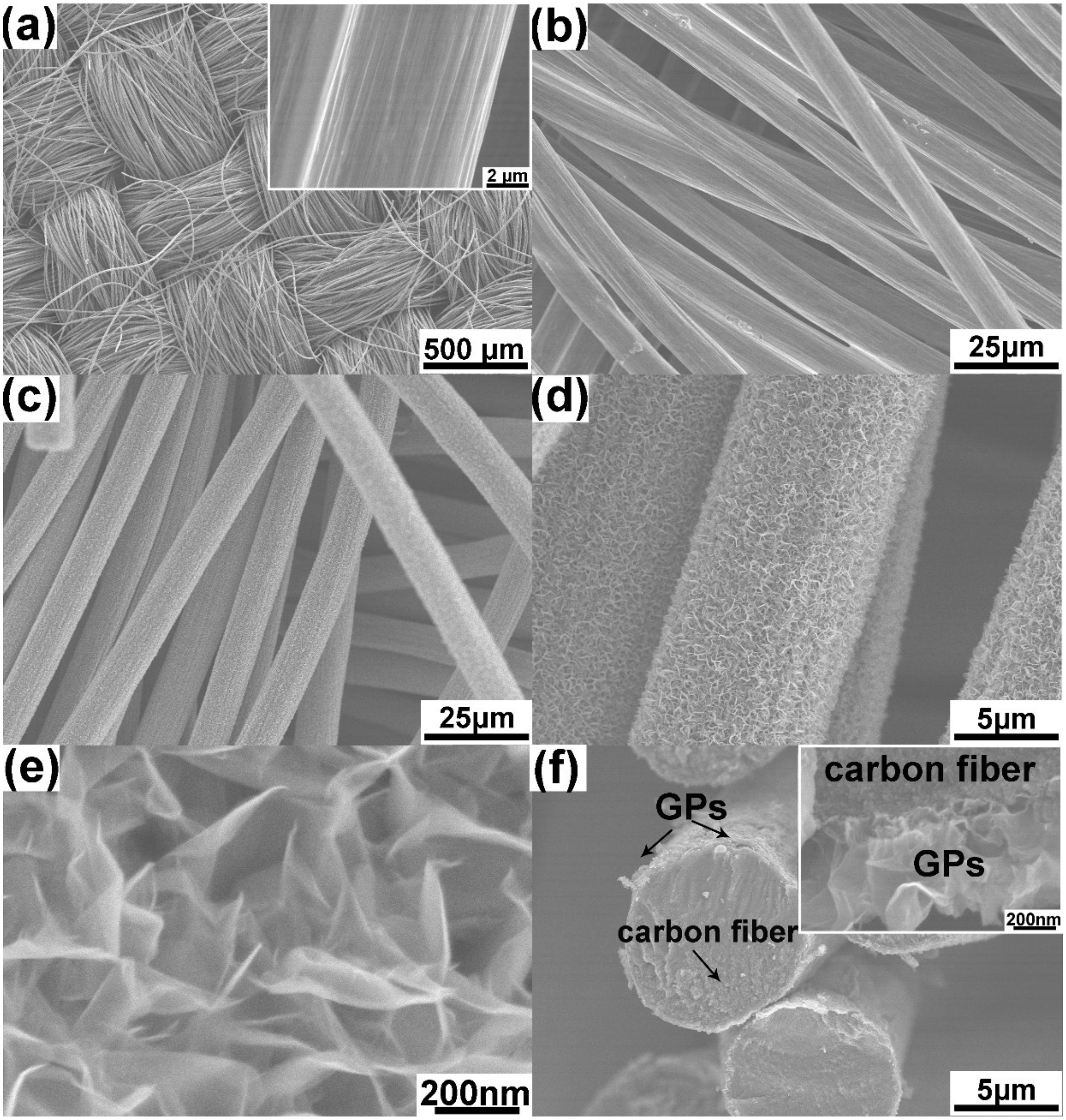

Fig. S4 SEM images. (a) CC at low magnification (the inset shows the surface of a single carbon fiber); (b) carbon fibers at low magnification; (c) uniform and large-scale coverage of GPs on carbon fibers; (d) carbon fibers covered by GPs at higher magnification; (e) high-magnification SEM image of GPs with sharp edges; (f) cross-sectional SEM image of carbon fibers covered by GPs (the inset displays the interface between carbon fiber and GPs).

SEM images of various surface morphologies of the CC/GPs/NCMTHs are shown in Fig. S5. The carbon fibers are uniformly covered by GPs/NCMTH nanoneedles (see Fig. S5a). The edges of GPs in the GPs/NCMTH structure can still be clearly distinguished (arrow indicated in Fig. S5b).

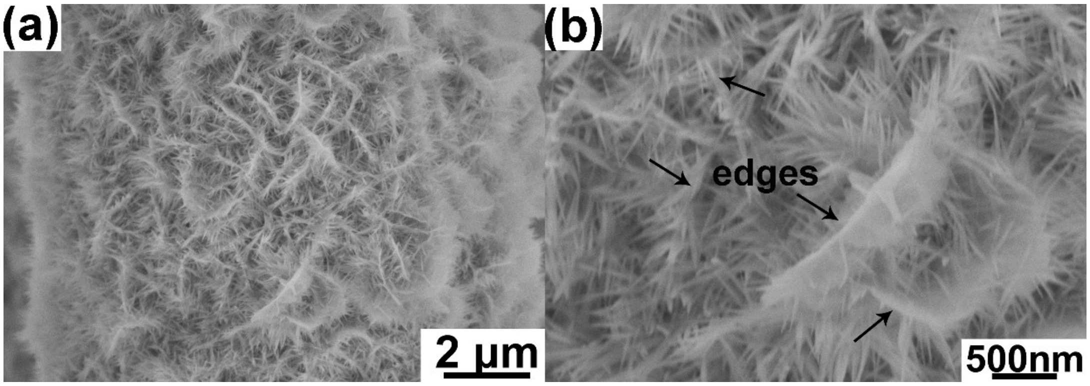

Fig. S5 SEM images of CC/GPs/NCMTHs: (a) low magnification; (b) high magnification.

The high-resolution TEM image of GPs is shown in Fig. S6. The thickness of a GP is approximately several nanometers, corresponding to tens of graphene layers with a planar lattice spacing of approximately 0.35 nm.

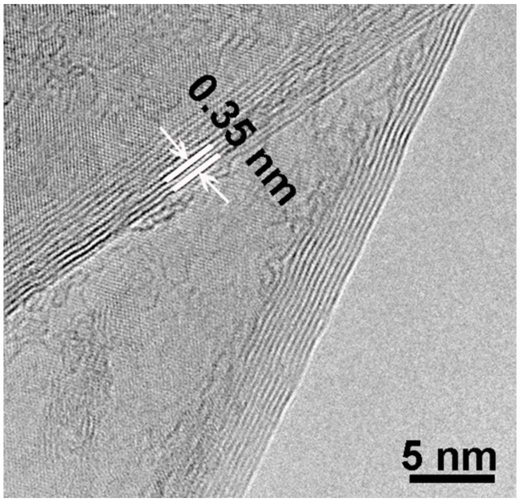

Fig. S6 high-resolution TEM image of GPs.

The Raman characterization of the graphene petals is provided in Fig.S7. The calculated I_D/I_G and I_{2D}/I_G ratios are 0.33 and 0.89, respectively, indicating that these graphene petals are highly graphitic.

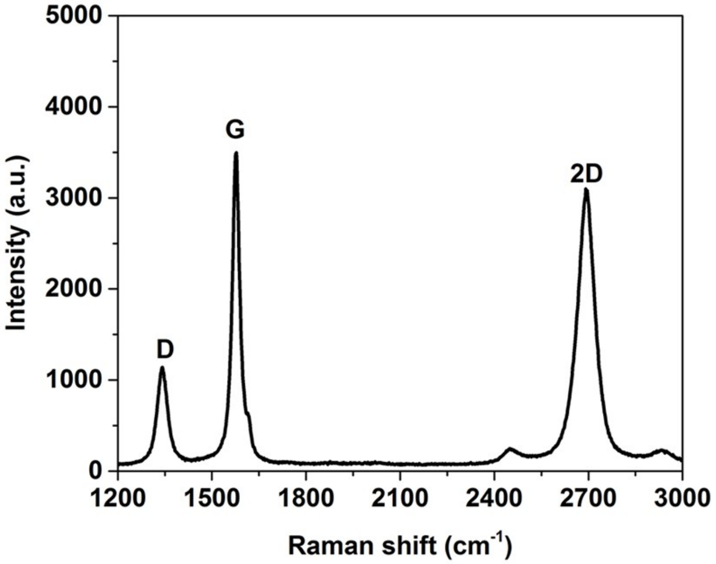

Fig. S7 Raman spectrum of GPs.

Fig. S8 contains SEM images of NCMTHs grown on pure CC. In Fig. S8a, the NCMTHs uniformly cover carbon fiber surface over a large scale. From the high-magnification image in Fig. S8b, these NCMTHs present a nanoneedle shape with a very sharp tip, similar to those grown on GPs.

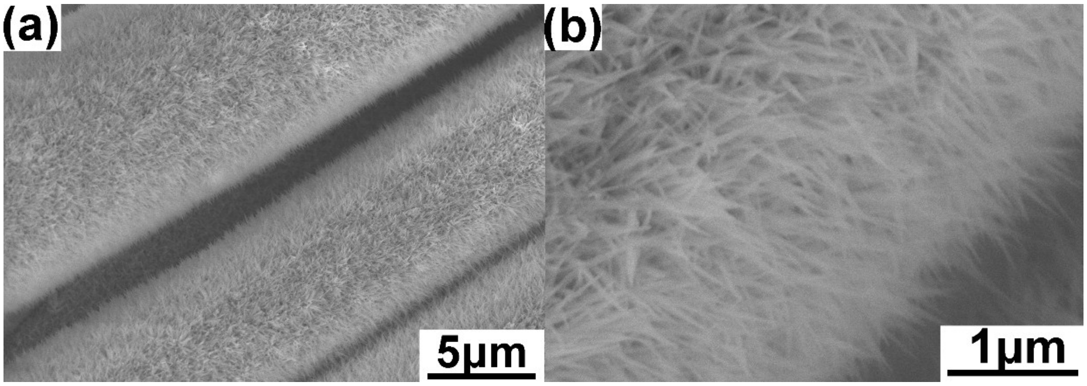

Fig. S8 SEM images of NCMTH nanoneedles grown on pure CC: (a) low-magnification image; (b) high-magnification image.

The contents of the elemental components in the hydroxide prepared in this work are estimated from the EDX mapping and shown in Table S1. The atomic ratio of Ni: Co: Mn: O in the as-prepared NCMTHs nanoneedles is estimated to be 5: 5: 1: 20. The composition is expected to be tunable by adjusting the concentrations of raw chemicals in the precursor solution during the preparation process.

Table S1. The atomic ratio of Ni: Co: Mn: O elements in NCMTHs

NCMTHs	Ni	Co	Mn	O
Designed	1	1	1	-
As-prepared	5	5	1	20

In the XPS of CC/GPs/NCMTHs (Fig. S9), the peaks located at 49.5, 284.5, 536.19, 642.3, 808.49 and 870.09 eV correspond to Mn_{3p}, C_{1s}, O_{1s}, Mn_{2p}, Co_{2p} and Ni_{2p}, respectively. This result further confirms the presence of Ni, Co, Mn, O and C elements on the surface of CC/GPs/NCMTHs.

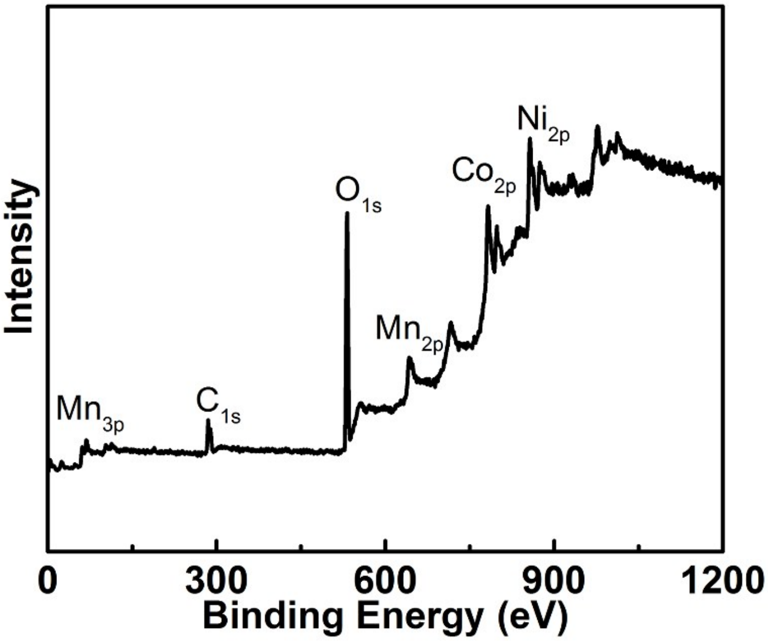

Fig. S9 XPS of CC/GPs/NCMTHs.

Based on XPS analysis, the atomic percentage of Ni, Co and Mn elements in NCMTHs is calculated to be 9.59%, 10.08% and 2.17% (see table S2), respectively.

Table S2. The atomic percentage of Ni, Co and Mn elements in NCMTHs

Elements	Atomic%
Ni	9.59
Co	10.08
Mn	2.17

Fig. S10 shows comparative Raman spectra of NCDHs and NCMTHs. In the NCDH Raman spectrum, the peaks at 458 cm^{-1} and 525 cm^{-1} are attributed to the stretching Ni-OH and Co-OH bonds.[10] However, the relative intensity of these peaks changes, and a new peak at approximately 650 cm^{-1} appears in the Raman spectrum of NCMTHs that might be attributed to the presence of Mn in the NCMTHs.

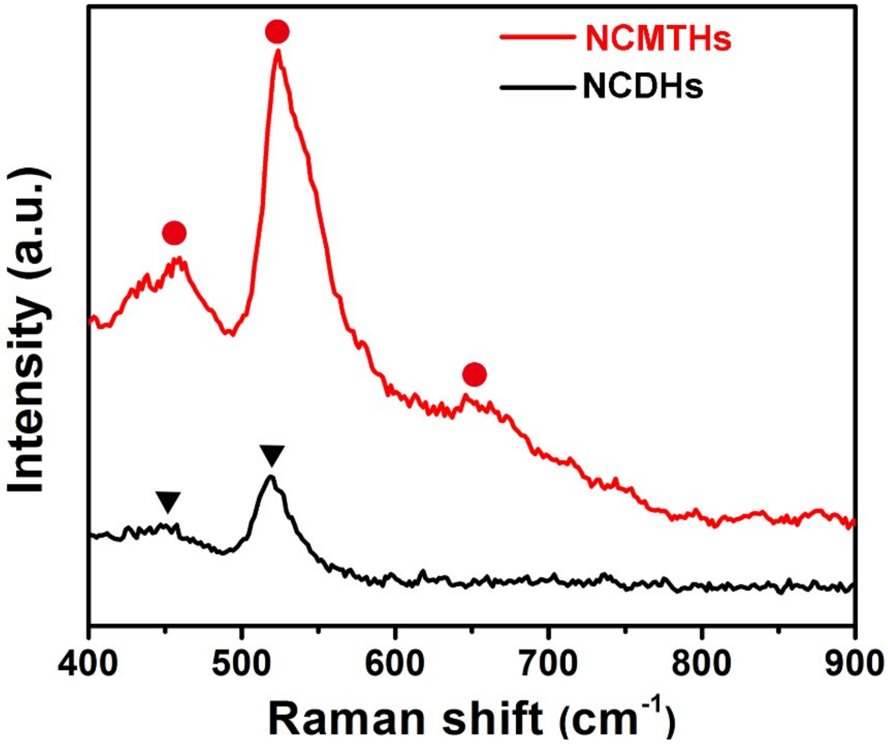

Fig. S10 Comparative Raman spectra of NCDHs and NCMTHs.

Fig. S11 shows galvanostatic charge/discharge profiles of CC/GPs/NCMTH electrodes at higher current densities ranging from 12 mA cm^{-2} to 100 mA cm^{-2} between 0 V to 0.4 V vs. SCE. Even at a current density as high as 100 mA cm^{-2}, the charge/discharge curves exhibit obvious voltage plateaus and remain relatively symmetric, suggesting a high rate capability of the CC/GPs/NCMTH electrodes.

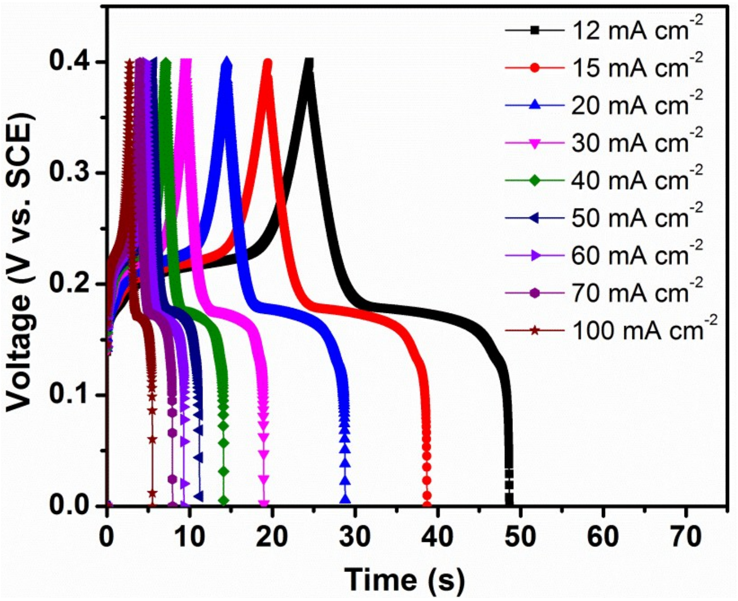

Fig. S11 Galvanostatic charge/discharge curves of CC/GPs/NCMTH electrodes at high current densities.

CV curves of CC/GPs/NCMTH, CC/NCMTH and CC/GPs/NCDH electrodes at the scan rate of 10 mV s^{-1} are shown in Fig. S12. The comparative CVs show distinct differences in intensities and shapes of the redox peaks, indicating the synergistic effect of GPs and NCMTHs during the redox reactions on the surface of the electroactive material.

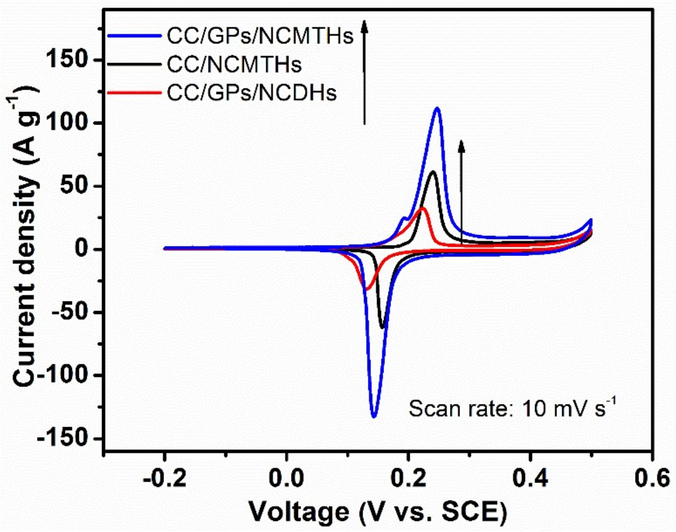

Fig. S12 Comparative CV curves of a CC/GPs/NCMTH, CC/ NCMTH and CC/GPs/NCDH hybrid electrodes at a scan rate of 10 mV s^{-1}.

The CV curves of CC/GPs/NCDH and CC/NCMTH electrodes in 2 M KOH electrolyte at scan rates from 5 to 100 mV s^{-1} are shown in Fig. S13. Compared to CC/GPs/NCMTH electrodes, the current densities of CC/GPs/NCDH electrodes (see Fig. S13a) and CC/NCMTHs (see Fig. S13b) electrodes are much smaller, further confirming the synergic effect of the THs and GPs on the enhanced overall electrochemical performance.

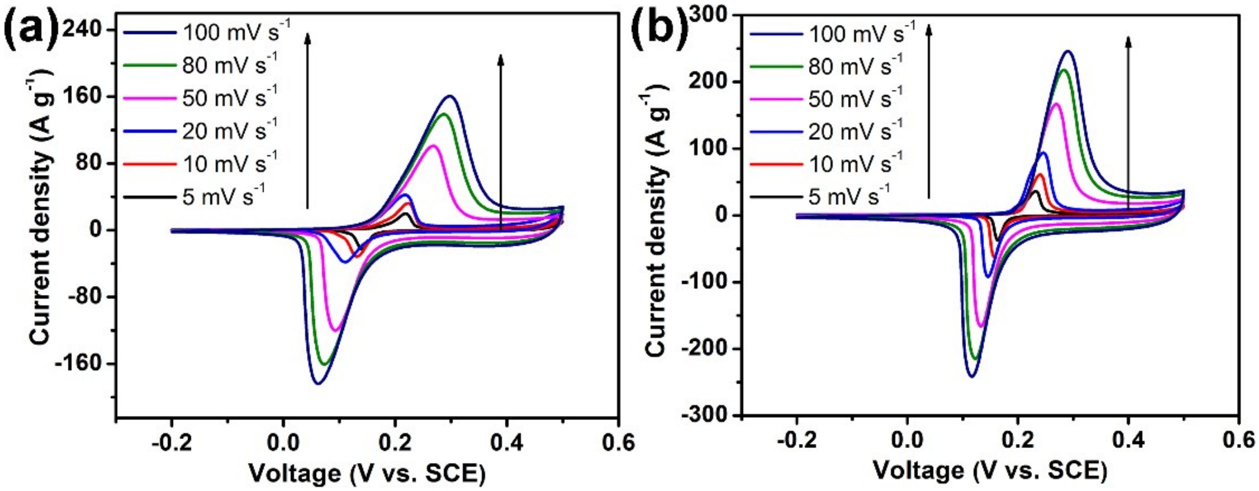

Fig. S13 CV curves of (a) CC/GPs/NCDH electrodes; (b) CC/NCMTH electrodes in 2 M KOH electrolyte at scan rates from 5 to 100 mV s^{-1}.

The impedance of the CC/NCMTH and CC/GPs/NCDH electrodes has been provided in Fig. S14. In Fig S14a, the R_e value is calculated to be 1.6 Ω for CC/NCMTH electrode. And for CC/GPs/NCDH electrode, the R_e value calculated from Fig. S14b is 1.7 Ω.

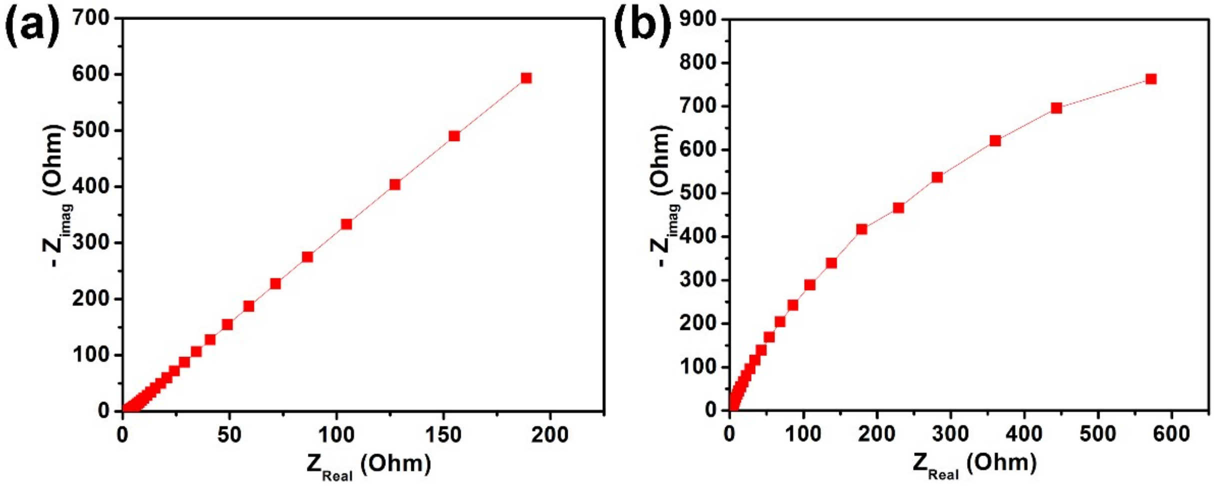

Fig.S14 Nyquist plot recorded from 0.1 Hz to 1 MHz for (a) CC/NCMTH and (b) CC/GPs/NCDH electrodes.

Fig. S15 indicates that the morphology of CC/GPs/NCMTH electrodes changes little after 3000 charge/discharge cycles. The nanoneedle shape of CC/GPs/NCMTHs remains intact, suggesting robust mechanical contact between the NCMTH nanoneedles and GPs during the long-term cycling.

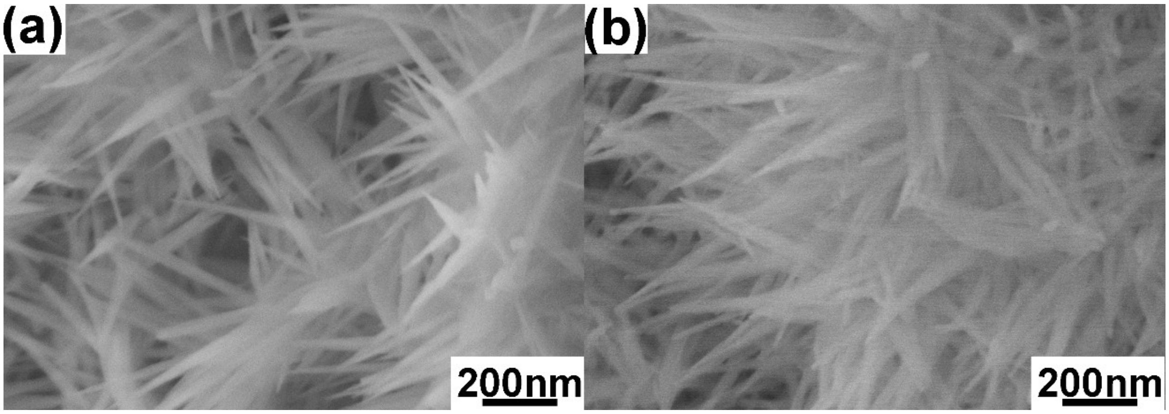

Fig. S15 SEM images of CC/GPs/NCMTH electrodes: (a) before and (b) after 3000 charge/discharge cycles.

For further comparison, the cyclic stabilities of CC/NCMTHs and CC/GPs/NCDH electrodes were tested at a current density of 10 mA cm^{-2} as shown in Fig. S16a and Fig. S16b, respectively. After 3000 charge/discharge cycles, the capacitance of CC/NCMTH electrodes experiences a gradual increase (with a capacitance retention of 112% based on the capacitance at the initial cycle), similar to that of CC/GPs/NCMTH electrodes. However, the capacitance of CC/GPs/NCDH electrodes increases slightly during the first 100 cycles and then decreases gradually with a capacitance retention of 94% after 3000 cycles of charging and discharging.

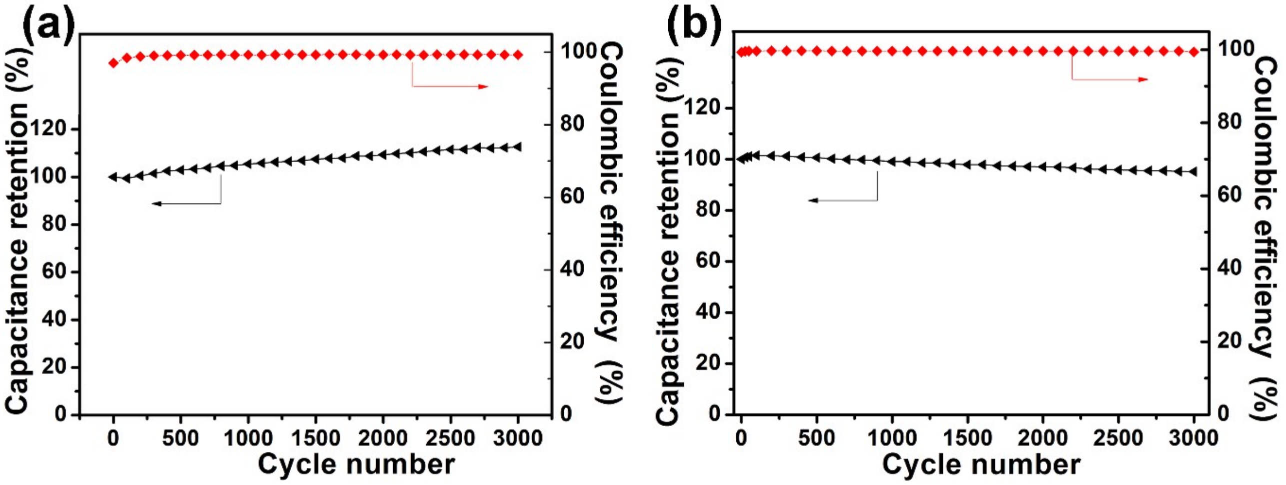

Fig. S16 Charge/discharge cyclic stability tests at a current density of 10 mA cm^{-2} and coulombic efficiencies during the tests: (a) CC/NCMTH electrodes; (b) CC/GPs/NCDH electrodes.

Fabrication of two-terminal asymmetric devices (CC/GPs//CC/GPs/NCMTHs): Asymmetric supercapacitor devices consisting of a chemically treated CC/GP negative electrode and a CC/GPs/NCMTH positive electrode were fabricated and tested. The negative electrode CC/GP was fabricated through the MPCVD process described in foregoing paragraphs and electrochemically activated in 0.5 M H_2SO_4 for 5 min, as described in prior work.[3] The asymmetric supercapacitor was assembled by sandwiching a commercial separator (Celgard™) between the positive and negative electrodes, and electrochemically characterized in a two-electrode configuration cell in 2 M KOH aqueous electrolyte solution. In order to achieve a stable potential window of 1.4 V, good long-term cyclic stability, and high charge transfer efficiency (coulombic efficiency), the mass of active negative and positive materials should be balanced. The stored charges (q) at negative and positive electrodes are related to the specific capacitance (C_s), the potential window (ΔV), and the mass (m) of the electrode according to $q = C_s \times \Delta V \times m$.[11] On the basis of the specific capacitance values and the potential windows of the active materials, the mass ratio of active negative and positive electrode materials (NCMTHs:GPs) is estimated to be ≈ 0.1 in these asymmetric supercapacitor devices.

Capacitance retention as a function of scan rate for a typical CC/GPs//CC/GPs/NCMTH two-terminal asymmetric supercapacitor device is shown in Fig. S17. The asymmetric supercapacitor device exhibits high capacitance retention of approximately 75% at 1000 mV s^{-1}, 60% at 3000 mV s^{-1} and 55% at 5000 mV s^{-1}, compared to that at 100 mV s^{-1} (approximately 0.2 F cm^{-2}), indicating a high rate capability for a two-terminal asymmetric supercapacitor device, substantially better than those of metal hydroxide-based asymmetric supercapacitors which fall in the range of 30 to 60% even at comparatively lower charge/discharge rates.[12-18]

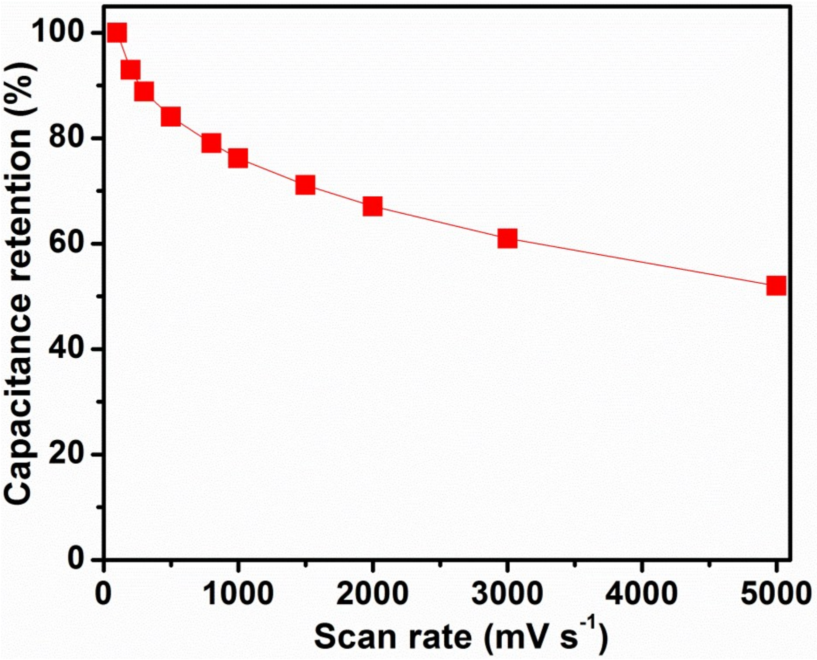

Fig. S17 Capacitance retention of the CC/GPs//CC/GPs/NCMTH two-terminal asymmetric supercapacitor devices.

A Nyquist plot for the CC/GPs//CC/GPs/NCMTH asymmetric supercapacitor devices is shown in Fig. S18. The real-axis intercept of the impedance spectrum at high frequencies in the Nyquist plot reflects ionic resistance of the electrolyte, intrinsic resistance of the active material, and contact resistance at the interface between the active material and current collector in the asymmetric supercapacitor device.[19] This value as calculated from Fig. S18 for the CC/GPs//CC/GPs/NCMTH asymmetric device is as low as 1.96 Ω. The semicircle in the high frequency region corresponding to charge transfer resistance R_{ct} is calculated to be 0.5 Ω from Fig. S18. This result suggests a very low internal resistance of the asymmetric devices, leading to high power and rate capability.

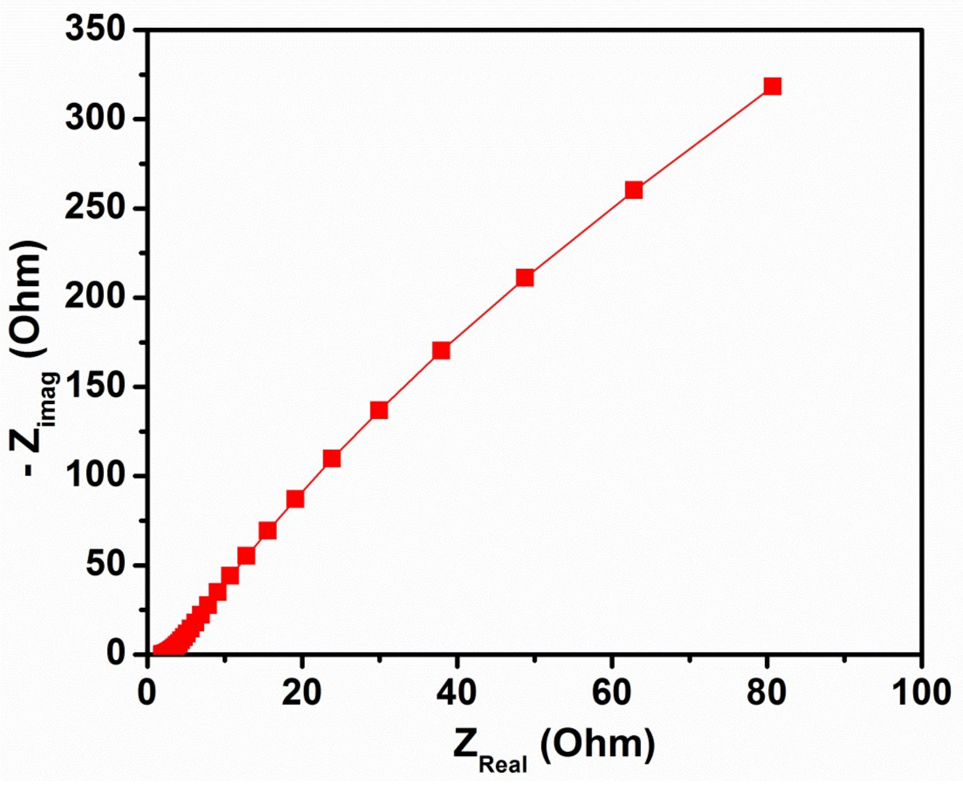

Fig. S18 Nyquist plot for the CC/GPs//CC/GPs/NCMTH asymmetric supercapacitor devices recorded from 0.1 Hz to 1 MHz.

Table S3. A summary of electrochemical performance of state-of-the-art pseudocapacitor electrodes based on metal hydroxides.

Materials	Rate capability	Energy density	Power density	Cycle stability	Refs.
α-$Co(OH)_2$	75% [a] (5~50 mV S^{-1})	-	-	76% (500)	20
β-$Co(OH)_2$ nanocone arrays	67% [a] (2~32 A g^{-1})	-	-	88% (3000)	21
Mesoporous $Co(OH)_2$ nanowire	60~87% (10~40 mA cm^{-2})	-	-	96% (1000)	22
β-$Co(OH)_2$	79.5% (0.5~2 A g^{-1})	-	-	-	23
mesoporous $Co(OH)_2$	-	-	-	81% (700)	24
$Ni(OH)_2$ nanoflakes	41%~55% [a] (1~100 mV S^{-1})	-	-	72%~79% (2000)	25
$Ni(OH)_2$ with open-ended nanotube	57% [a] (1~10 A g^{-1})	-	-	-	26
$Ni(OH)_2$/graphene	30% (1~50 mV S^{-1})	13.5	15.2	94.3% (3000)	12
$Ni(OH)_2$/graphene	71% [a] (2.8~45.7 A g^{-1})	37	10	No obvious decreases (2000)	27
Porous $Ni(OH)_2$/graphene	41% [a] (2~20 mV S^{-1})	94	1.2	95.7% (2000)	28
$Ni(OH)_2$/hydrogel graphene	50.1% (5~40 A g^{-1})	-	-	95% (1000)	29
Hexagonal platelet $Co(OH)_2$/graphene	67% (2~10 A g^{-1})	24.3	3.5	94% (500)	30
$Ni(OH)_2$/carbon nanotubes	67% (2.5~50 mA cm^{-2})	32.5	1.8	83% (3000)	31
$Ni(OH)_2$/carbon nanotubes/graphene	63% [a] (1~20 A g^{-1})	-	-	80% (500)	32

$Ni(OH)_2$/ Ni foam	9% [a] (4~16 A g^{-1})	-	-	52% (300)	33
$Co(OH)_2$ nanoflakes/Ni foam	76.4% (1~40 A g^{-1})	-	-	76.7% (2000)	34
$Co(OH)_2$/graphene/Ni foam	72% [a] (2~32 A g^{-1})	-	-	91% (3000)	35
$Ni(OH)_2$ nanowire/ MnO_2 nanoflakes	40.6% (0.5~20 A g^{-1})	20	10	97% (3000)	36
$Ni(OH)_2$ on graphite foam	70% (0.5~10 A g^{-1})	-	-	65% (1000)	37
$Ni(OH)_2$ nanoflakes on graphite nanosheets	55.6% [a] (3~60 A g^{-1})	-	-	93% (550)	38
Co-Ni DHs/$NiCo_2O_4$ on carbon fiber paper	53.25%~74.14% (2~90 mA cm^{-2})			68%~81% (2000)	10
$Ni_{0.25}Co_{0.75}(OH)_2$ nanoarrays	81% (5~50 mA cm^{-2})	-	-	85% (1000)	39
$Ni(OH)_2$–$Co(OH)_2$ composites	63.3% (2~20 A g^{-1})	-	-	84.7% (1000)	40
nickel-cobalt hydroxide nanorod arrays	70% (20~200 mV S^{-1})	-	-	91% (1000)	41
Ni–Co binary hydroxide	60.5%~73.3%[a] (3~15 A g^{-1})			97.3% (1000)	17
Nickel-cobalt hydroxide nanosheets	62% (0.9~35.7 A g^{-1})	-	-	83% (2000)	42
Nickel-cobalt hydroxide/ Ni foam	66.1% (30 A g^{-1})	-	-	86% (1000)	43
CC/GPs/ NCMTH nanoneedles	95.5% (1 to 100 mA cm^{-2})	30	39	117% (3000)	This work

[a] estimated from the given information in the literature.

REFERENCES

1. G. P. Xiong, K. P. S. S. Hembram, D. N. Zakharov, R. G. Reifenberger and T. S. Fisher, *Diam Relat Mater*, 2012, 27-28, 1-9.
2. G. P. Xiong, C. Z. Meng, R. G. Reifenberger, P. P. Irazoqui and T. S. Fisher, *Adv Energy Mater*, 2014, 4, 1300515.
3. G. P. Xiong, C. Z. Meng, R. G. Reifenberger, P. P. Irazoqui and T. S. Fisher, *Energy Technology*, 2014, 2, 897-905.
4. G. P. Xiong, K. P. S. S. Hembram, R. G. Reifenberger and T. S. Fisher, *J Power Sources*, 2013, 227, 254-259.
5. Q. F. Wang, X. F. Wang, B. Liu, G. Yu, X. J. Hou, D. Chen and G. Z. Shen, *J Mater Chem A*, 2013, 1, 2468-2473.
6. G. P. Xiong, C. Z. Meng, R. G. Reifenberger, P. P. Irazoqui and T. S. Fisher, *Electroanal*, 2014, 26, 30-51.
7. P. Simon and Y. Gogotsi, *Nat Mater*, 2008, 7, 845-854.
8. S. L. Zhang and N. Pan, *Adv Energy Mater*, 2015, 5, 1401401.
9. T. Sato, G. Masuda and K. Takagi, *Electrochim Acta*, 2004, 49, 3603-3611.
10. L. Huang, D. Chen, Y. Ding, S. Feng, Z. L. Wang and M. Liu, *Nano Lett*, 2013, 13, 3135-3139.
11. V. Khomenko, E. Raymundo-Pinero and F. Beguin, *J Power Sources*, 2006, 153, 183-190.
12. J. Yan, Z. J. Fan, W. Sun, G. Q. Ning, T. Wei, Q. Zhang, R. F. Zhang, L. J. Zhi and F. Wei, *Adv Funct Mater*, 2012, 22, 2632-2641.
13. Z. Tang, C. H. Tang and H. Gong, *Adv Funct Mater*, 2012, 22, 1272-1278.
14. J. Y. Ji, L. L. Zhang, H. X. Ji, Y. Li, X. Zhao, X. Bai, X. B. Fan, F. B. Zhang and R. S. Ruoff, *Acs Nano*, 2013, 7, 6237-6243.
15. J. W. Lang, L. B. Kong, M. Liu, Y. C. Luo and L. Kang, *J Solid State Electr*, 2010, 14, 1533-1539.
16. X. Wang, A. Sumboja, M. F. Lin, J. Yan and P. S. Lee, *Nanoscale*, 2012, 4, 7266-7272.
17. X. Sun, G. K. Wang, H. T. Sun, F. Y. Lu, M. P. Yu and J. Lian, *J Power Sources*, 2013, 238, 150-156.
18. H. Chen, L. F. Hu, Y. Yan, R. C. Che, M. Chen and L. M. Wu, *Adv Energy Mater*, 2013, 3, 1636-1646.
19. J. Gamby, P. L. Taberna, P. Simon, J. F. Fauvarque and M. Chesneau, *J Power Sources*, 2001, 101, 109-116.
20. T. Zhao, H. Jiang and J. Ma, *J Power Sources*, 2011, 196, 860-864.
21. F. Cao, G. Pan, P. Tang and H. Chen, *J Power Sources*, 2012, 216, 395-399.
22. C. Yuan, X. Zhang, L. Hou, L. Shen, D. Li, F. Zhang, C. Fan and J. Li, *J Mater Chem*, 2010, 20, 10809-10816.
23. S. Tang, S. Vongehr, Y. Wang, L. Chen and X. Meng, *Journal of Solid State Chemistry*, 2010, 183, 2166-2173.
24. C. Yuan, X. Zhang, B. Gao and J. Li, *Mater Chem Phys*, 2007, 101, 148-152.
25. H. Jiang, T. Zhao, C. Li and J. Ma, *J. Mater. Chem.*, 2011, 21, 3818-3823.
26. M.-S. Wu and K.-C. Huang, *Chem Commun*, 2011, 47, 12122-12124.
27. H. Wang, H. S. Casalongue, Y. Liang and H. Dai, *Journal of the American Chemical Society*, 2010, 132, 7472-7477.
28. J. Yan, W. Sun, T. Wei, Q. Zhang, Z. Fan and F. Wei, *J Mater Chem*, 2012, 22, 11494-11502.
29. S. Chen, J. Duan, Y. Tang and S. Zhang Qiao, *Chem-Eur J*, 2013, 19, 7118-7124.
30. D. Ghosh, S. Giri and C. K. Das, *ACS Sustainable Chemistry & Engineering*, 2013, 1, 1135-1142.
31. Z. Tang, C.-h. Tang and H. Gong, *Adv Funct Mater*, 2012, 22, 1272-1278.
32. L. L. Zhang, Z. Xiong and X. S. Zhao, *J Power Sources*, 2013, 222, 326-332.
33. G.-W. Yang, C.-L. Xu and H.-L. Li, *Chem. Commun.*, 2008, 6537-6539.
34. G. X. Pan, X. Xia, F. Cao, P. S. Tang and H. F. Chen, *Electrochim Acta*, 2012, 63, 335-340.

35. C. Zhao, X. Wang, S. Wang, Y. Wang, Y. Zhao and W. Zheng, *Int J Hydrogen Energ*, 2012, 37, 11846-11852.
36. H. Jiang, C. Li, T. Sun and J. Ma, *Chem Commun*, 2012, 48, 2606-2608.
37. J. Ji, L. L. Zhang, H. Ji, Y. Li, X. Zhao, X. Bai, X. Fan, F. Zhang and R. S. Ruoff, *Acs Nano*, 2013, 7, 6237-6243.
38. X. Wang, Y. Wang, C. Zhao, Y. Zhao, B. Yan and W. Zheng, *New Journal of Chemistry*, 2012, 36, 1902-1906.
39. W. Zhu, Z. Lu, G. Zhang, X. Lei, Z. Chang, J. Liu and X. Sun, *J Mater Chem A*, 2013, 1, 8327-8331.
40. J. Li, M. Yang, J. Wei and Z. Zhou, *Nanoscale*, 2012, 4, 4498-4503.
41. R. R. Salunkhe, K. Jang, S.-w. Lee and H. Ahn, *Rsc Adv*, 2012, 2, 3190-3193.
42. M. Wang, J. Xue, F. Zhang, W. Ma and H. Cui, *Journal of Nanoparticle Research*, 2015, 17, 1-9.
43. J. Pu, Y. Tong, S. B. Wang, E. H. Sheng and Z. H. Wang, *J Power Sources*, 2014, 250, 250-256.